Catheter ablation lesion visualization with intracardiac strain imaging in canines and humans

Vincent Sayseng, Julien Grondin, Vasant Salgaonkar, Christopher S. Grubb, Maryam Basij, Mohammad Mehrmohammadi, Vivek Iyer, Daniel Wang, Hasan Garan, Elaine Y. Wan, Elisa Konofagou

Abstract—Catheter ablation is a common treatment for arrhythmia, but can fail if lesion lines are non-contiguous. Identification of gaps and non-transmural lesions can reduce the likelihood of treatment failure and recurrent arrhythmia. Intracardiac myocardial elastograph is a strain imaging technique that provides visualization of the lesion line. Lesion size estimation and gap resolution was evaluated in an open chest canine model (n=3), and clinical feasibility was investigated in patients undergoing ablation to treat typical cavotricuspid isthmus atrial flutter (n=5). A lesion line consisting of three lesions and two gaps was generated in each canine left ventricle via epicardial ablation. One lesion was generated in one canine right ventricle. Average lesion and gap areas were measured with high agreement (33 ± 14 mm^2 and 30 ± 15 mm^2, respectively) when compared against gross pathology (34 ± 19 mm^2 and 26 ± 11 mm^2, respectively). Gaps as small as 11 mm^2 (3.6 mm on epicardial surface) were identifiable. Absolute error and relative error in estimated lesion area were 9.3 ± 8.4 mm^2 and 31 ± 34 %; error in estimated gap area was 11 ± 9.0 mm^2 and 40 ± 29 %. Flutter patients were imaged throughout the procedure. Strain was shown to be capable of differentiating between baseline and after ablation completion as confirmed by conduction block. In all patients, strain decreased in the cavotricuspid isthmus after ablation (mean paired difference of -17 ± 11 %, $p < 0.05$). IME could potentially become a useful ablation monitoring tool in the clinic.

Index Terms—ablation, electrophysiology, lesion monitoring, strain imaging, intracardiac echocardiography.

I. INTRODUCTION

CATHETER ablation is one of the most effective treatments for atrial and ventricular arrhythmias [1]–[3]. An ablation catheter deposits energy in specific areas of the heart to form a barrier of non-conductive tissue that interrupts the electrical circuit responsible for the arrhythmia. The lesion line must be contiguous; gaps between lesions or non-transmural lesions can serve as a pathway of conductive tissue through which the arrhythmia circuit can recover, leading to treatment failure [4]–[7].

Currently, lesion geometry and location is estimated by using surrogate parameters (e.g. force-time integral or FTI, and contact force) that have been found to correlate with lesion size, in conjunction with an electroanatomic mapping system [8]–[10]. These parameters are indirect measurements of lesion formation, which limits their accuracy. Furthermore, the inherent variance in atrial volume, tissue deformation from application of the ablation catheter to the endocardial surface, and unexpected procedural complications can cause significant errors in the integration of the electroanatomic map with the CT and MRI images, leading to inaccurate lesion localization [11], [12]. Given that the single-procedure success of catheter ablation of persistent atrial fibrillation is estimated to be as low as 25% [13], there is an urgent need for an ablation monitoring technique capable of accurately and robustly depicting myocardial anatomy and lesion formation that can easily be integrated into the clinical routine.

Ultrasound-based lesion mapping methods are a promising means of obtaining real-time feedback during ablations. Unlike MRI-based lesion mapping techniques—which would require extensive adjustments in the current procedure workflow due to the required additional hardware and technicians—ultrasound (particularly intracardiac echocardiography or ICE) is already a common imaging modality during ablations[12], [14]. A novel ablation catheter with near field ultrasound imaging capabilities has been shown capable of providing realtime feedback about lesion formation [15]. While an improvement over the current state-of-the art catheters which relay contact force or FTI, the catheter cannot provide information about the position of lesions relative to one another. Photoacoustic imaging of ablation has been investigated, but thus far reports have been limited to benchtop experiments with ex-vivo tissue [16]–[19]. Elastography-based methods employing shear waves or acoustic radiation force impulse (ARFI) to identify lesions based on its mechanical moduli are an area of active research.

Shear wave approaches have yet to investigate lesion gap resolution [20], [21], and ARFI has stringent requirements regarding the imaging configuration in terms of depth and catheter orientation relative the myocardial wall [22].

Intracardiac Myocardial Elastography (IME) is a strain-based lesion mapping technique developed by our group. An ICE catheter employs a high-frame rate acquisition sequence to estimate strain in the atrial or ventricular walls. IME has minimal hardware requirements, and theoretically can be programmed onto any ultrasound system capable of high-frame rate acquisitions. Grondin et al demonstrated feasibility by capturing strain images in the canine LA, and by observing that ablation lead to reduced local strain in the ablated region of the human atria in atrial fibrillation patients [23]. Bunting et al used IME in the canine LV to detect lesion gaps of 15 mm and 45 mm *in vivo* [24].

This paper presents the next stage of development in the IME. Its objectives are twofold: 1) investigate lesion area and lesion gap resolution in an open-chest canine model, and 2) explore the potential diagnostic utility of IME strain in a clinical feasibility study. Lesion gap resolution was investigated by creating lesion lines comprised of three epicardial lesions and two gaps in three canine left ventricles (LV). In patients, IME was used to monitor ablation in the cavotricuspid isthmus (CTI) throughout an atrial flutter procedure in five subjects.

II. METHODS

A. Animal model experimental protocol

Due to its cellular, functional, and physiological similarities with the human heart, the canine heart is one of the most popular large animal models in cardiac research [25]. Furthermore, since mongrel canines are genetically diverse, they are close representations to the non-homogenous genetic background of humans [26].

The study protocol was approved by the Institutional Animal Care and Use Committee (IACUC) at Columbia University, and was compliant with the Public Health Service Policy on Humane Care and Use of Laboratory Animals. Lateral thoracotomy was performed on anesthesized mongrel canines (n = 3, 100% male, 26 ± 2.1 kg) to expose the myocardium for epicardial ablation. The intracardiac ultrasound catheter (Carto Soundstar, Biosense Webster, Irvine, CA, USA) was introduced via the external jugular vein and advanced through the superior vena cava. Positioning the probe in the right ventricle (RV) provided images of the anterior and antero-lateral segments of the left ventricle (LV). Imaging of the RV was performed by positioning the probe in the LV via apical puncture.

Epicardial lesions were created in the LV and RV by catheter ablation (Carto 3 System, Biosense Webster, Irvine, CA, USA). In the LV, a lesion line consisting of three lesions with two gaps were generated in three animals. In the RV, one lesion was created in one animal. Images were acquired prior to and after each lesion (SoundStar 10 F Catheter, Biosense Webster, Irvine, CA, USA). For the LV lesion lines, images were acquired at baseline, and then after each lesion for a total of four time points. For the RV lesion, images were acquired before and after the ablation.

Lesions were imaged with one of two ultrasound platforms (the same catheter, Soundstar, was employed). Two canines (two LV lesions lines and one RV lesion) were imaged with an Acuson SC2000 in research mode (Siemens, Munich, Germany). The transmit sequence consisted of 24 steered plane waves (virtual source located >300 mm behind the transducer) at a frame rate of 200-250 fps and depth of 80 mm. The angular aperture of the field-of-view was 70°. One canine (one LV lesion line) was imaged with a Verasonics Vantage (WA, USA) and a modified Acuson Swiftlink Connector (TransducerWorks, PA, USA). A high-frame rate compounded sequence was employed (15 virtual sources, focus located 21 mm behind the transducer, 460 fps, depth 80 mm, angular aperture 90°) [27].

At the conclusion of the procedure, the myocardium was excised. The lesion line was segmented and placed in the freezer (-18° C) for 40-60 minutes. The sample was sliced transmurally along the axis of the lesion line. Sections were submerged in 1% tetrazolium chloride (TTC) and placed in an incubator (37°) for at least 40 minutes. TTC stained the lesions white. Photos of the sections with scale bar for reference were obtained (Nikon EOS Rebel T3i, Tokyo, Japan).

B. Human experimental protocol

The study protocol was approved by the Institutional Review Board (IRB) of Columbia University. Patients were informed of the study's risk prior to obtaining consent. The transmit sequence complied with the U.S. Food and Drug Administration (FDA) limits on acoustic output.

Patients with typical cavotricuspid isthmus atrial flutter (n = 5, men = 60%, age = 67 ± 16 years old) undergoing RF ablation of the cavotricuspid isthmus of the right atrium (RA) were imaged with an ICE clinical machine in research mode (ViewMate ICE Catheter and Viewmate Z, Abbott, Chicago, IL). The ICE catheter was positioned in the RA. A custom transmit sequence was implemented: 1.5s of conventionally focused imaging at 30 fps, followed by 1 s of a single diverging wave sequence (-6.5 mm virtual source, 600 fps frame rate). The latter acquisition was used to estimate myocardial displacement and strain; the former was used to provide a B-mode reference frame of end-systole over which to overlay the strain. The ICE ultrasound field-of-view was set to the CTI region proximal to the tricuspid valve. Images were acquired prior, during, and after the CTI ablation procedure. The ultrasound view was updated throughout the procedure to ensure that the ablation catheter was in view before, during, and after each lesion. The ablation procedure was considered complete once achievement of block was confirmed via coronary sinus pacing.

C. Intracardiac Myocardial Elastography (IME) imaging

Three different ultrasound platforms were used in this study: Siemens Acuson, Verasonics Vantage, and Abbott Viewmate Z. Each hardware platform possessed different strengths. The Acuson provides a means to coregister the lesion line and the ICE view through the CARTOSOUND software (Carto 3 System, Biosense Webster, Irvine, CA, USA), which can mark the position of the ablation catheter in real time when it is in plane with the ICE catheter [28]. The Vantage's open programmability allows for the implementation of optimal high frame rate strategies. The Viewmate Z is a clinically available FDA-approved scanner electrophysiologists have experience operating. Beamforming, displacement estimation, and strain estimation parameters slightly differed between the three platforms.

Beamforming was performed internally with the Acuson. Raw RF data obtained with the Vantage and Viewmate Z was beamformed by delay-and-sum [27].

For data obtained with the Viewmate Z and Vantage, axial displacements were calculated from beamformed RF signals using a 1-D normalized cross-correlation kernel [29]. Due to its lower achievable acquisition frame rate, axial displacements were estimated from the beamformed envelope (as opposed to RF) signals on data obtained from the Acuson. For the canine imaging protocol, the displacements observed in the LV and RV were accumulated throughout LV systole, and RV systole, respectively. In the human protocol, the displacements were accumulated during atrial filling, a segment of the cardiac cycle during which the CTI lengthens. Different phrases of the cardiac cycle were imaged in the animal and human models to preserve the directionality of the strain being observed, i.e. positive strain was estimated in both. Axial strains were derived from cumulative axial displacements with a 1-D least-squares estimator (LSQSE) [30]. Strain images were smoothed using a 2-D median filter. The specific processing parameters used with each hardware platform—displacement kernel, strain (LSQSE) kernel, and median filter kernel—are summarized in a table in the Appendix (Table A.1).

D. Canine study – image analysis and statistics

Canine strain images were validated against gross pathology. The images of the TTC-stained, excised lesion line were converted to grayscale, scaled, aligned with ICE, and overlaid onto the B-mode image based on anatomical landmarks (Fig. 1). TTC stains the lesions white; in grayscale, the lesions are brighter compared to non-ablated myocardium. The lesions were masked by a combination of brightness thresholding and manual segmentation (Fig. 1).
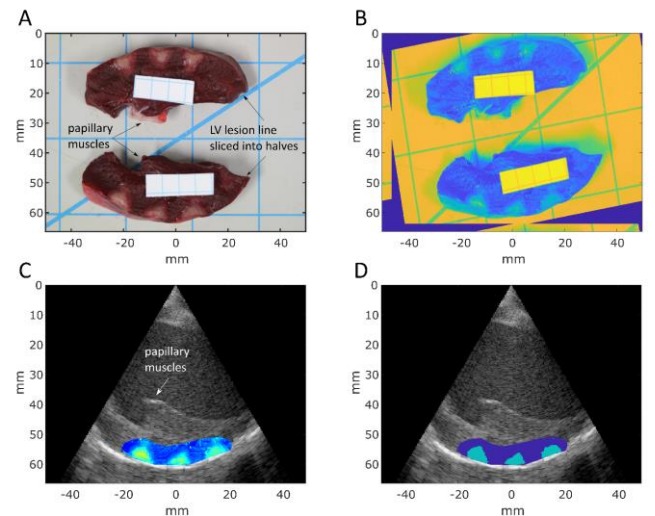

Fig. 1. Coregistration procedure to validate IME lesion maps with gross pathology in canines. The lesion line was excised from the myocardium after sacrifice and sliced transmurally along the axis of the lesion line to provide a cross-sectional view of the lesion and gap area (A). Using anatomical markers (e.g. papillary muscles and epicardial surface), the intensity image was manually rotated and translated (B) to coregister with the B-mode image (C). Intensity thresholding and manual segmentation were employed to create a binary mask that indicated the lesion area by gross pathology (indicated in light blue) (D).

Due to translation and deformation of the myocardium during the cardiac cycle, the lesion line may move out of the field-of-view at certain time points during systole. This drop-out is evident upon examination of the strain movie through the entirety of systole. Thus, the number of displacement frames accumulated varied for each acquisition. The strain magnitude is dependent on the number of displacement frames accumulated. The strain image dynamic range was adjusted accordingly in order to maintain high image contrast between unablated and ablated tissue. The upper bound of the dynamic range (DR_{upper}) was empirically chosen to be half of the median strain at baseline at the number of frames accumulated:

$$DR_{upper} = \frac{median\big(\varepsilon_{baseline}(n)\big)}{2} \qquad (1)$$

where $\varepsilon_{baseline}(n)$ is the masked strain values in the nth accumulated frame at baseline. The lower bound of the dynamic range was set to 0%.

Lesion area as estimated by IME was calculated as follows:

$$A_{strain}(mm) = A_{pixel} * \sum_{i=1}^{N} \begin{cases} 0 & if\ \varepsilon(i) \geq \varepsilon_{thresh} \\ 1 & if\ \varepsilon(i) < \varepsilon_{thresh} \end{cases}, \qquad (2)$$

where $\varepsilon(i)$ represents strain at a given pixel i within a masked region consisting of N pixels, ε_{thresh} is the strain threshold, and A_{pixel} is the area of each pixel in mm. Masks were manually delineated to isolate lesions (n=10) and gaps (n=6). The boundary of the gap masks was set by a vector spanning the apex of the two lesions, at the points closest to the endocardial wall. The other borders consisted of the lesion perimeters and

the epicardial wall. The absolute (δA) and relative difference between A_{strain} and the areas reported by gross pathology (A_{gross}) were calculated, given

$$A_{gross}(mm) = A_{pixel} * \sum_{i=1}^{N} \begin{cases} 0 & if \ pixel(i) \geq pixel_{thresh} \\ 1 & if \ pixel(i) < pixel_{thresh} \end{cases}. \quad (3)$$

The brightness threshold $pixel_{thresh}$ was determined empirically based on qualitative assessment of the gross pathology images, and A_{pixel} is the area of each pixel in mm. Manual segmentation was performed to isolate individual lesion areas.

The threshold under which a point would be considered a lesion, ε_{thresh}, was empirically derived. The Dice similarity coefficient (DSC) ranges from 0 to 1, and measures the similarity between two binary sets. A DSC of 1 indicates that the binary masks are identical, while a score of 0 indicates that there is no intersection between the positive values in the binary masks. The DSC has frequently been employed in medical imaging analysis (e.g. to compare manual segmentation against an automated method) [31], [32]. In terms of true positives (TP), false positives (FP), and false negatives (FN), the DSC between two binary sets A and B is given by,

$$dice(A, B) = \frac{2TP}{2TP+FP+FN}. \quad (4)$$

In this study, TP corresponds to tissue that was ablated and correctly identified as such by IME, FP corresponds to regions of unablated tissue that was incorrectly identified as ablated, and FN corresponds to ablated tissue that was incorrectly identified as unablated.

The DSC of the lesion maps produced by strain imaging and gross pathology (the ground truth) were compared for a range of ε_{thresh}, defined as,

$$\varepsilon_{thresh} = \alpha * median(\boldsymbol{\varepsilon}_{baseline}(n)), \quad (5)$$

with α evaluated within the range of [0, 1.5]. The α value that yields the optimal ε_{thresh} was determined by calculating the mean DSC curve across the four lesion lines. The α value corresponding to the maximum of the mean DSC was chosen to calculate ε_{thresh} in the canine model.

E. Human study – image analysis and statistics

The CTI was manually segmented. Median axial strain was calculated within the CTI for the five patients. Median strain (ε_{median}) at the CTI at baseline and at the conclusion of the procedure (once block was achieved) was statistically compared via the Student's paired t test. In contrast to the canine protocol, no thresholding was performed to isolate individual lesions, and the dynamic range was set to [-40%, 40%] for all cases.

III. RESULTS

A. Open chest canine ablation

ME was capable of accurately capturing the formation of the LV lesion line throughout the ablation procedure (Fig. 2). At baseline, LV strain was homogenously positive and high magnitude ($\varepsilon \geq DR_{upper}$) throughout (Fig. 2A). In contrast, lesions manifested as regions of low strain ($\varepsilon < \frac{DR_{upper}}{2}$). The strain images demonstrate the progression of lesion line formation, lesion-by-lesion (Fig. 2b-d). At the conclusion of the ablation experiment, three distinct lesions and two distinct gaps are visible (Fig. 2d).

The contours of the lesion areas as indicated by the TTC-stained tissue sections (shown in green) were overlaid onto the post-ablation strain-based lesion maps (Fig. 3). Qualitatively, there is good agreement between the lesions detected by ME and the gross pathology. In each of the three LV lesion lines, ME correctly identified three lesions and two gaps. The singular lesion in the RV was also correctly identified.

Calculating the DSC across a range of α values (Eq. 3) yielded the plot summarized in Fig. 4. The maximum of the mean DSC curve was found at $\alpha = 0.27$, wherein a DSC value of 0.62 was found.

The lesion and gap areas as determined by IME versus gross pathology are summarized in Fig. 5. The lesion areas are designated in turquoise, with the gaps indicated in yellow. Qualitatively, the thresholded strain lesion maps compare well against the gross pathology. The lesion areas found by strain and gross pathology are summarized and compared in Table I. Gap area assessment is summarized in Table II.

By gross pathology, the lesion and gap areas (A_{gross}) measured 34 ± 19 mm² and 26 ± 11 mm² on average, respectively. By IME strain imaging, the lesion areas and gaps (A_{strain}) were estimated to be 33 ± 14 mm² and 30 ± 15 mm² on average, respectively.

The individual difference in lesion area between strain and gross pathology (δA) ranged 0.82-24 mm², with a mean difference of 9.3 ± 8.4 mm². In terms of relative error, the difference ranged 3.9 - 120 %, with a mean relative difference of 31 ± 34 %.

The individual difference in gap areas between strain and gross pathology ranged 0.63 – 23 mm², with a mean difference of 11± 9.0 mm². In relative error, the difference ranged 5.5 – 78 %, with a mean relative difference of 40 ± 29 %.

B. Atrial flutter CTI ablation

Lesion mapping in a patient receiving CTI ablation to relieve atrial flutter is demonstrated in Fig. 6. Images were acquired at baseline (Fig. 6A), during (Fig. 6B), and after (Fig. 6C) CTI ablation. The lesion line was initiated proximal to the tricuspid valve, and progressed towards the direction distal the tricuspid valve during the ablation. At baseline, the CTI exhibits homogenously positive, high-magnitude strain (i.e. strain greater than about 20%) (Fig. 6a). During the procedure, strain

374 in the region proximal the tricuspid valve is low magnitude (i.e.
375 strain less than about 20%), while the region distal the valve
376 (thus far in the procedure unablated) still possesses high-
377 magnitude positive strain (Fig. 6b). Finally, the entire CTI is
378 observed to have low-magnitude strain at the conclusion of the
379 ablation procedure (Fig. 6c).
380   In all five patients imaged, ε_{median} in the CTI decreased after
381 ablation compared to baseline. The mean paired difference in
382 CTI strain was -17 ± 11 %. Employing a two-sided paired t-test,
383 the difference was determined to be statistically significant (p <
384 0.05).
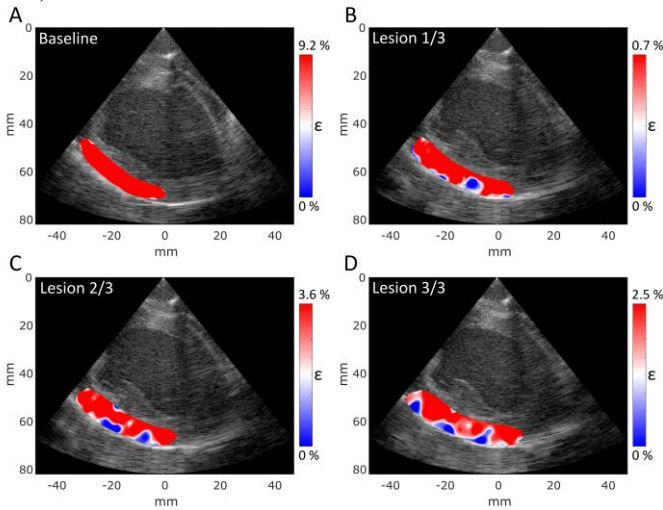
385
386 Fig. 2. Strain-based lesion maps obtained with ICE imaging. IME imaged the
387 development of a lesion line generated in an open-chest canine via epicardial
388 ablation. Unablated myocardium exhibits high-magnitude positive strain over
389 systole, indicated in red. At baseline, prior to any ablations, high-magnitude
390 strain is evident throughout the LV wall (A). Ablated tissue is stiff and non-
391 contractile, manifesting as low-magnitude regions, indicated in blue. IME
392 accurately tracked the ablation lesion-by-lesion: the first lesion is indicated in
393 (B), followed by a second lesion and the first gap in (C), and finally all three
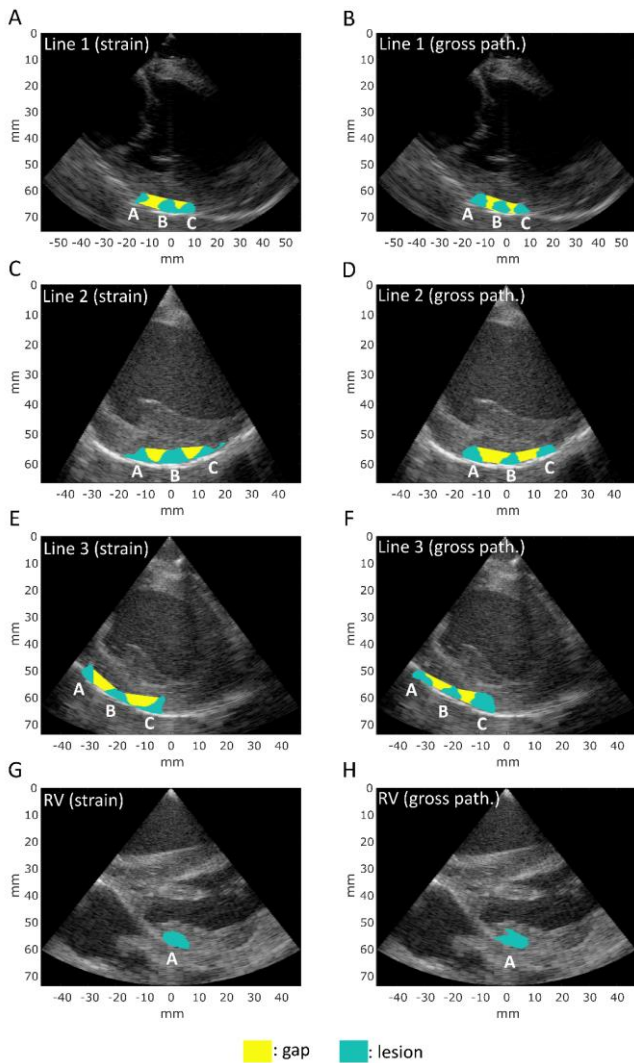394 lesions and both gaps in (D).

395
396
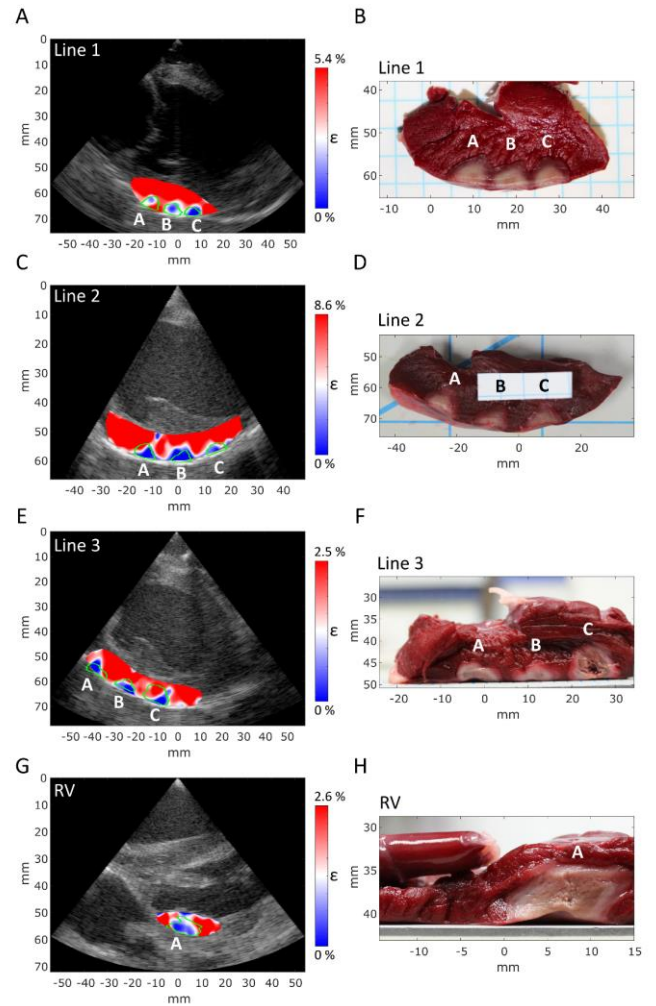
397
398 Fig. 3. Post-ablation IME lesion maps compared against gross pathology. Three
399 lesion lines consisting of three lesions and two gaps were generated in the
400 canine LV (n=3) (A-F); one lesion was generated in the canine RV (n=1) (G-
401 H). The contour of the lesions area according to the gross pathology cross-
402 section is outlined in green and overlaid onto the lesion maps. IME successfully
403 identified all the lesions (n=10) and gaps (n=6) that were generated in the canine
404 model.

405
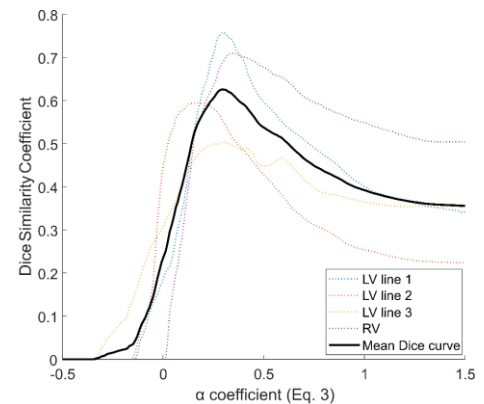
406
407 Fig. 4. Dice similarity coefficient (DSC) for each lesion line. The metric
408 measures the similarity between two binary images, with higher values
409 indicating more similarity. The three lesion lines and one RV lesion were
410 evaluated against gross pathology. A range of α values [-0.5, 1.5] were
411 evaluated to determine the optimal strain threshold, ε_{thresh} (Eq. 3). The
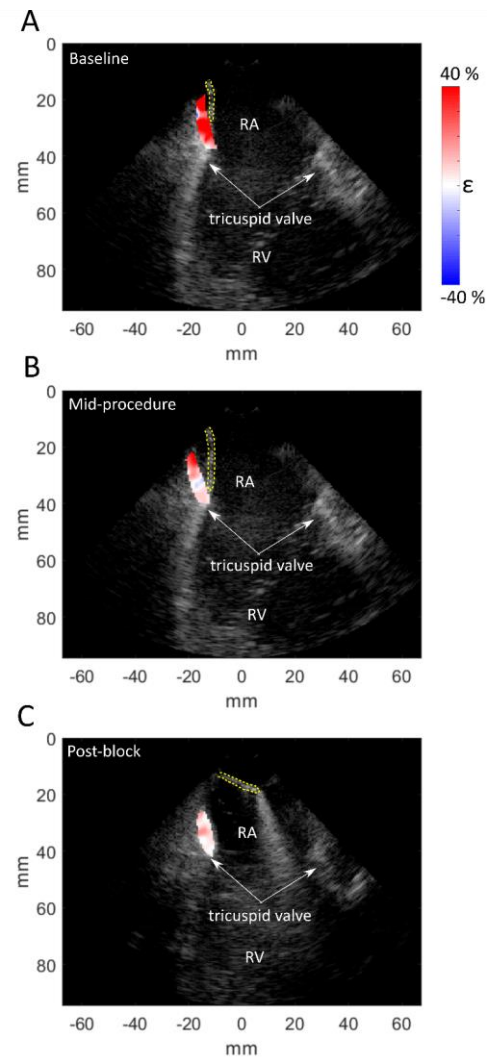412 maximum DSC of the mean Dice curve occurs at $\alpha = 0.27$.

413

Fig. 5. Thresholded strain-based lesion maps versus gross pathology. $A_{strain}(\alpha = 0.27)$ for the lesion and gaps detected by IME were assessed against the ground truth areas according to gross pathology (A_{gross}) for LV lesion line 1 (A, B), LV lesion line 2 (C, D), LV lesion line 3 (E, F), and the RV lesion (G, H). Lesion areas are indicated in turquoise, with gap areas in yellow.

TABLE I
LESION AREA BY IME STRAIN AND GROSS PATHOLOGY IN THE CANINE

Lesion	A_{gross} (mm^2)	A_{strain} (mm^2)	δA (mm^2)	Relative error (%)
Line 1, Lesion A	28	15	13	46
Line 1, Lesion B	27	34	7.9	30
Line 1, Lesion C	18	23	4.8	26
Line 2, Lesion A	30	28	2.1	7.0
Line 2, Lesion B	20	45	24	120
Line 2, Lesion C	21	22	0.82	3.9
Line 3, Lesion A	29	28	1.1	3.9
Line 3, Lesion B	26	32	6.8	26
Line 3, Lesion C	65	42	23	35
RV, Lesion A	72	62	9.5	13
Mean	34	33	9.3	31
STD	19	14	8.4	34

TABLE II
GAP AREA BY IME STRAIN AND GROSS PATHOLOGY IN THE CANINE

Gap	A_{gross} (mm^2)	A_{strain} (mm^2)	δA (mm^2)	Relative error (%)
Line 1, Gap AB	19	32	13	66
Line 1, Gap BC	11	11	0.63	5.5
Line 2, Gap AB	43	25	18	43
Line 2, Gap BC	25	22	3.2	13
Line 3, Gap AB	29	39	10	35
Line 3, Gap BB	30	53	23	78
Mean	26	30	11	40
STD	11	15	9.0	29

Fig. 6. Tracking ablation of the cavotricuspid isthmus (CTI) in the RA of a patient with atrial flutter. The catheter is outlined by a yellow dotted line. Unablated myocardium in the CTI exhibits high-magnitude (>20%) positive strain (indicated in red) over the atrial filling phase of the cardiac cycle. Ablated tissue manifests as comparatively low magnitude (<20%) or near-zero magnitude strain (indicated in pink or white). At baseline, the CTI is observed as healthy throughout (A). Lesions were first generated proximal to the tricuspid valve. There is a clear difference in strain magnitude between the ablated tissue proximal the valve and the unablated tissue distal the valve (B). At the end of the ablation procedure, the CTI is observed to have low-magnitude strain throughout (C).
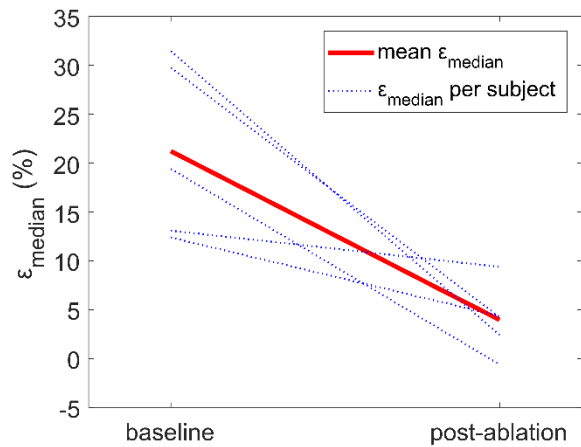
Fig. 7. Median strain within the CTI decreases after ablation. Patients receiving ablation of the CTI to relieve atrial flutter were imaged with IME (n=5). Median strain decreased for all patients, with a statistically significant difference in the mean paired difference (paired Student's t-test, * <0.05).

IV. DISCUSSION

The potential of IME for lesion and gap visualization and quantification with intracardiac echocardiography was investigated. Employing an open-chest canine model, IME was capable of resolving all ten lesions and all six lesion gaps generated in three LVs and one RV. IME was then used to track atrial flutter ablation in human subjects. There was a reduction in strain in the ablated region (the CTI) in all five patients after the ablation procedure.

In both the canine and clinical studies, lesions manifested as areas of low-magnitude or near-zero percent strain, as opposed to areas of negative strain. The mechanics behind non-compliant and compliant passive myocardial tissue dictates the directionality of the strain. Following acute ischemia, the affected region of the myocardium becomes passive [33]. During systole, the compliant ischemic tissue stretches, exhibiting negative strain. In RF catheter ablation, the mechanism is different. The lesion that is generated is non-compliant, and becomes stiffer compared to unablated tissue [34]. Since non-compliant, stiff tissue does not deform easily, 0% strain is expected over both systole (as shown in the canine model) and diastole (as shown in the patient model).

The strain magnitude within the ablated area was significantly reduced compared to unablated tissue in the canine. The dynamic range as defined in Eqn. 1 was chosen to increase the visual contrast between scar and unablated tissue; healthy tissue manifests as regions of high magnitude positive strain (in red) while scarred tissue manifests are regions of low magnitude strain (in blue) (Fig. 2). These low-magnitude strain regions were indicative of non-contractile scar tissue, verified by overlaying the ground truth lesion contours as defined by gross pathology (Fig. 3). Qualitatively, there was excellent agreement between the IME lesion maps and the gross pathology: IME correctly represented the three lesions in each canine LV as a non-contiguous linear line (Fig. 3A-F).

Thresholding was employed to allow for quantitative comparison of lesion and gap area between strain imaging and gross pathology (Tables I and II). The strain threshold under which a region of tissue should be classified as scar was chosen based on the peak mean Dice curve (Fig. 4). Thresholding can also be a useful tool for visualization, simplifying interpretation of the strain images. The optimal hard threshold will likely be variable among patients, imaging conditions, and the heart chamber being imaged. However, given that lesions are stiff and non-compliant, it can be hypothesized that lesion strain magnitude should always be close to zero. Future clinical studies should be conducted to determine the degree of variation in the strain threshold between patients. If the variability is small, a general threshold may be implemented instead of adjusting the value for each patient.

Gap resolution was improved compared to previous implementations of IME. In earlier work by our group, the smallest detectable gap measured from lesion edges at the epicardial level was 15 mm [24]. This study demonstrated that IME was capable of resolving gaps as small as 11 mm^2, or 3.6 mm measured edge-to-edge at the epicardial level (Table II, Line 1 Gap BC, Fig. 5A-B). The improved lesion mapping is due to the implementation of superior high frame-rate transmit strategies. Instead of a single-diverging wave sequence, a 15-source compounding (Verasonics) and 23-source composite plane wave sequence (Siemens) were applied in the canine model. Increased gap resolution improvement is likely attributable to improved SNR and lateral resolution over single-source diverging wave imaging [35], [36].

Great care was taken to best align the lesion line and ultrasound plane in the canine model. In conjunction with SOUNDSTAR, the Acuson was able to graphically mark the location of the ablation catheter when it was in-plane. In the acquisitions taken with the Vantage, each potential location was manually palpated prior to ablation; if the location was in-plane, the resulting tissue deformation would be evident in the B-mode. Nonetheless, an inherent source of error in the canine study design is that a 2-D strain image of a live tissue target featuring 3-D translation and deformation was compared against a 2-D section of gross pathology. A lower degree of agreement in the lesion and gap areas are attributable to the imperfect coregistration of the two 2-D representations of the lesion line. This imperfect coregistration likely inflated the error of the lesion and gap area estimation—31 ± 34 % and 40 ± 29 %, respectively (Table I and II)—and led to a relatively low maximum DSC of 0.62. In future large animal studies, the addition of Gadolinium-enhanced Magnetic Resonance Imaging could mitigate this source of error [37]. The combination of MRI 3-D visualization of lesion line and gross pathology would allow for more reliable assessment of lesion and gap area accuracy, and provide insight on how much error is attributable to poor coregistration versus the resolution limitations of IME.

The feasibility of IME in intracardiac echocardiography as a useful diagnostic tool was investigated via a pilot study comparing the strain in the CTI before and after atrial flutter ablation. Strain was calculated during atrial filling of the RV, during which the CTI exhibits extension (i.e. stretches). Scar

548 tissue is stiffer and less compliant [38]; ablated regions of the
549 atrial wall exhibit significantly reduced extension during atrial
550 filling, manifesting as regions of low-magnitude strain (<20%)
551 in IME lesion maps. The progression of a CTI ablation is
552 summarized in Fig. 6. The ablation catheter begins proximal the
553 valve and progresses along the CTI in the direction distal the
554 valve, the location of previous lesions clearly indicated by the
555 strain drop compared to the baseline. IME was able to
556 differentiate between the CTI before and after ablation (mean
557 $\Delta \varepsilon = -17 \pm 11$ %), with every patient recording a decrease in
558 ε_{median} at the end of the procedure (Fig. 7).

559 The clinical pilot study demonstrated that IME could be
560 integrated into the current ablation workflow with minimal
561 adaptations, especially since the use of ICE is standard of care
562 in many cardiac ablation procedures. Many of the proposed
563 approaches to imaging the lesion line require additional
564 hardware, such as MRI [12], [14], or an additional probe to
565 induce a push beam [21], [38], [39]. In contrast, IME was
566 integrated into an ICE platform that was already being used in
567 ablation procedures at the EP clinic. Furthermore, IME can
568 provide a large and deep field-of-view of the lesion line in
569 contrast to photoacoustic [16]–[18] or ARFI [38], [39] methods,
570 allowing for quicker assessment of an ablation procedure's
571 progress.

572 In contrast to the canine study, the IME was unable to
573 observe the development of the lesion line lesion-by-lesion.
574 Due to constraints on the programmability of the Abbott ICE
575 platform's research mode, a single diverging wave transmit
576 sequence was employed, as opposed to the compounding or
577 composite plane wave sequences used in the canine protocol.
578 The reduced imaging SNR, as well as the lower thickness of the
579 human RA compared to the canine LV and RV, lead to poorer
580 strain resolution and less precise lesion maps.

581 As stated in the Methods section, the displacement estimation
582 algorithm employed depended on the hardware platform that
583 was used to collect the acquisitions. Similarly to previous
584 iterations of IME [23], [24], displacement estimation was
585 performed using 1-D cross-correlation on the RF data derived
586 from the Verasonics Vantage and Abbott Viewmate Z. In
587 contrast, 1-D cross-correlation was performed on the *envelope*
588 of the RF signal on data derived from the Siemens Acuson
589 system. RF-based motion estimators are generally considered
590 more accurate than envelope-based estimators at high frame
591 rates, since the former contains phase information [40]–[42].
592 However, RF-based estimators can perform poorly if the
593 acquisition frame rate is too low, or a large window size is
594 employed, due to decorrelation from false peak or jitter errors
595 [41], [43]. The Siemens Acuson transmit sequence frame rate
596 used herein (≤ 250 Hz) was substantially lower than that of the
597 Verasonics (460 Hz) or Abbott (600 Hz) systems. Envelope-
598 based displacement estimation was necessary as limitations in
599 the programmability of the Acuson prevented imaging at higher
600 frame rates. Preliminary analysis confirmed that the envelope-
601 based estimator would be preferred for the Siemens data, given
602 the frame rate limitations. While displacement estimation on RF
603 versus beamformed envelope signals is comparable in the
604 canine study, the latter approach is less optimal because it

605 requires a larger displacement window size (Table A.1). When
606 imaging thin tissue such as the atria, a large displacement kernel
607 precludes high resolution imaging. Finally, 1-D cross-
608 correlation of the envelope signal was performed instead of
609 using a 2-D kernel, which is more common [41], [44]. It was
610 hypothesized that a 1-D kernel would be more accurate due to
611 the edge mismatch between adjacent plane waves in the
612 transmit sequence, visible in the B-mode (Fig 1C, 1D, for
613 example). While this mismatch in the lateral direction would
614 lead to substantial decorrelation when employing a 2-D kernel,
615 this artifact is not relevant when using a uniaxial estimator.

616 There are some limitations to consider and future work that
617 must be performed before IME is integrated into the clinic. The
618 implementation of IME described here only estimated 1-D
619 (axial) motion. In both the canine and human study, ultrasound
620 views were chosen such that the predominate direction of
621 myocardial motion was in the axial direction. However, prior to
622 implementation in the clinic, integration of 2-D or 3-D motion
623 estimation is necessary to circumvent angle dependence in the
624 strain calculation.

625 IME requires that the ultrasound plane is well-aligned with
626 the lesion line. Due to the myocardial translation and rotation
627 inherent in the cardiac cycle, this can be a challenging demand
628 for the ICE operator. Furthermore, this study evaluated IME's
629 performance in monitoring ablation of the CTI, a region of the
630 myocardium that is particularly amenable to ICE imaging.
631 Imaging regions of the myocardium that are frequently ablated,
632 such as the pulmonary veins in atrial fibrillation ablation, is
633 more challenging. A future clinical implementation of IME
634 could be integrated with an electroanatomic system. The
635 clinical model could be improved by using the Acuson platform
636 and SOUNDSTAR software, which is capable of visually
637 tagging the ablation catheter when it is view, leading to better
638 alignment with the lesion line. Linking IME to an
639 electroanatomic system could theoretically allow for the
640 generation of stain lesion maps that are registered to specific
641 positions in the myocardium, allowing for a pseudo-3D
642 visualization. Alternatively, a 3D ICE catheter could be
643 employed.

644 This study investigated gap resolution in the canine LV.
645 Clinically, ablation in the atria are more common than ablation
646 in the ventricles. Unfortunately, the smaller size of the canine
647 atrial chamber compared to the human equivalent complicated
648 navigation of the ICE catheter, and good coregistration of the
649 lesion line and ultrasound windows was unattainable.
650 Furthermore, lesions are typically generated on the endocardial
651 wall, as opposed to the epicardial wall as performed in the
652 canine protocol. Further studies are needed to investigate the
653 gap resolution of IME in thinner myocardial tissue and in
654 endocardial catheter ablation.

655 Although three different ultrasound platforms were used in
656 this study, determining the optimal hardware platform for IME
657 is outside the scope of this paper. We hypothesize that any
658 platform capable to achieving high frame rate imaging and
659 integration with electroanatomic mapping systems would
660 enable IME to be a diagnostic tool of high clinical value.

661

V. CONCLUSION

The potential of IME to visualize the lesion line and better inform ablation procedures was investigated. Gap resolution of IME lesion mapping was validated in an open-chest canine model that tracked epicardial ablations in the ventricles, with the smallest gap tested being 11 mm^2 (3.6 mm on epicardial surface). A clinical feasibility study was also performed to demonstrate the diagnostic utility of strain, and to show that IME could be integrated into ablation procedures with minimal modifications to the current workflow. Additional feasibility in animals and humans are warranted to prove that IME is a viable ablation monitoring approach for atrial arrhythmias.

VI. APPENDIX

TABLE A. I
ULTRASOUND PLATFORM PROCESSING PARAMETERS

Ultrasound platform	Probe center freq. (MHz)	Disp. kernel (mm)	Disp. kernel overlap (%)	Strain (LSQSE) kernel (mm)	2D median filter kernel (mm, °)
Verasonics Vantage	5.2	3.9	90	4.3	(2.1, 2.5)
Siemens SC2000 Acuson	6.0	4.8	90	3.0	(4.6, 2.9)
Abbott Viewmate Z	6.0	1.0	90	2.3	(1.4, 2.3)

VII. ACKNOWLEDGEMENTS

VIII. REFERENCES

[1] S. M. Al-Khatib *et al.*, "2017 AHA/ACC/HRS Guideline for Management of Patients With Ventricular Arrhythmias and the Prevention of Sudden Cardiac Death: A Report of the American College of Cardiology/American Heart Association Task Force on Clinical Practice Guidelines and the Heart Rhythm Society," *J. Am. Coll. Cardiol.*, vol. 72, no. 14, pp. e91–e220, 02 2018, doi: 10.1016/j.jacc.2017.10.054.

[2] H. Calkins *et al.*, "2017 HRS/EHRA/ECAS/APHRS/SOLAECE expert consensus statement on catheter and surgical ablation of atrial fibrillation," *Heart Rhythm*, vol. 14, no. 10, pp. e275–e444, 2017, doi: 10.1016/j.hrthm.2017.05.012.

[3] R. L. Page *et al.*, "2015 ACC/AHA/HRS Guideline for the Management of Adult Patients With Supraventricular Tachycardia: Executive Summary: A Report of the American College of Cardiology/American Heart Association Task Force on Clinical Practice Guidelines and the Heart Rhythm Society," *Circulation*, vol. 133, no. 14, pp. e471-505, Apr. 2016, doi: 10.1161/CIR.0000000000000310.

[4] M. A. Miller *et al.*, "Acute electrical isolation is a necessary but insufficient endpoint for achieving durable PV isolation: the importance of closing the visual gap," *Europace*, vol. 14, no. 5, pp. 653–660, May 2012, doi: 10.1093/europace/eus048.

[5] S. P. Thomas, E. M. W. BSc, and D. L. Ross, "The Effect of a Residual Isthmus of Surviving Tissue on Conduction after Linear Ablation in Atrial Myocardium," *J Interv Card Electrophysiol*, vol. 4, no. 1, pp. 273–281, Feb. 2000, doi: 10.1023/A:1009838201448.

[6] Ranjan Ravi *et al.*, "Gaps in the Ablation Line as a Potential Cause of Recovery From Electrical Isolation and Their Visualization Using MRI," *Circulation: Arrhythmia and Electrophysiology*, vol. 4, no. 3, pp. 279–286, Jun. 2011, doi: 10.1161/CIRCEP.110.960567.

[7] S. J. Melby *et al.*, "Atrial fibrillation propagates through gaps in ablation lines: Implications for ablative treatment of atrial fibrillation," *Heart Rhythm*, vol. 5, no. 9, pp. 1296–1301, Sep. 2008, doi: 10.1016/j.hrthm.2008.06.009.

[8] A. Thiagalingam *et al.*, "Importance of catheter contact force during irrigated radiofrequency ablation: evaluation in a porcine ex vivo model using a force-sensing catheter," *J. Cardiovasc. Electrophysiol.*, vol. 21, no. 7, pp. 806–811, Jul. 2010, doi: 10.1111/j.1540-8167.2009.01693.x.

[9] D. C. Shah, H. Lambert, H. Nakagawa, A. Langenkamp, N. Aeby, and G. Leo, "Area under the real-time contact force curve (force-time integral) predicts radiofrequency lesion size in an in vitro contractile model," *J. Cardiovasc. Electrophysiol.*, vol. 21, no. 9, pp. 1038–1043, Sep. 2010, doi: 10.1111/j.1540-8167.2010.01750.x.

[10] P. M. Kistler *et al.*, "The Impact of CT Image Integration into an Electroanatomic Mapping System on Clinical Outcomes of Catheter Ablation of Atrial Fibrillation," *Journal of Cardiovascular Electrophysiology*, vol. 17, no. 10, pp. 1093–1101, 2006, doi: 10.1111/j.1540-8167.2006.00594.x.

[11] E. K. Heist *et al.*, "Factors affecting error in integration of electroanatomic mapping with CT and MR imaging during catheter ablation of atrial fibrillation," *J Interv Card Electrophysiol*, vol. 17, no. 1, pp. 21–27, Oct. 2006, doi: 10.1007/s10840-006-9060-2.

[12] C. Knackstedt, P. Schauerte, and P. Kirchhof, "Electro-anatomic mapping systems in arrhythmias," *Europace*, vol. 10, no. suppl_3, pp. iii28–iii34, Nov. 2008, doi: 10.1093/europace/eun225.

[13] S. Brooks *et al.*, "Insights into ablation of persistent atrial fibrillation: Lessons from 6-year clinical outcomes," *Journal of Cardiovascular Electrophysiology*, vol. 29, no. 2, pp. 257–263, Feb. 2018, doi: 10.1111/jce.13401.

[14] C. Eitel, G. Hindricks, M. Grothoff, M. Gutberlet, and P. Sommer, "Catheter Ablation Guided by Real-Time MRI," *Curr Cardiol Rep*, vol. 16, no. 8, p. 511, Jun. 2014, doi: 10.1007/s11886-014-0511-6.

[15] M. Wright *et al.*, "Characteristics of Radiofrequency Catheter Ablation Lesion Formation in Real Time In Vivo Using Near Field Ultrasound Imaging," *J Am Coll Cardiol EP*, vol. 4, no. 8, pp. 1062–1072, Aug. 2018, doi: 10.1016/j.jacep.2018.04.002.

[16] S. Iskander-Rizk, P. Kruizinga, A. F. W. van der Steen, and G. van Soest, "Spectroscopic photoacoustic imaging of radiofrequency ablation in the left atrium," *Biomed Opt Express*, vol. 9, no. 3, pp. 1309–1322, Feb. 2018, doi: 10.1364/BOE.9.001309.

[17] N. Dana, L. Di Biase, A. Natale, S. Emelianov, and R. Bouchard, "In vitro photoacoustic visualization of myocardial ablation lesions," *Heart Rhythm*, vol. 11, no. 1, pp. 150–157, Jan. 2014, doi: 10.1016/j.hrthm.2013.09.071.

[18] G. A. Pang, E. Bay, X. L. Deán-Ben, and D. Razansky, "Three-dimensional optoacoustic monitoring of lesion formation in real time during radiofrequency catheter ablation," *J. Cardiovasc. Electrophysiol.*, vol. 26, no. 3, pp. 339–345, Mar. 2015, doi: 10.1111/jce.12584.

[19] S. Iskander-Rizk *et al.*, "Real-time photoacoustic assessment of radiofrequency ablation lesion formation in the left atrium," *Photoacoustics*, vol. 16, p. 100150, Dec. 2019, doi: 10.1016/j.pacs.2019.100150.

[20] W. Kwiecinski *et al.*, "Quantitative evaluation of atrial radio frequency ablation using intracardiac shear-wave elastography," *Med Phys*, vol. 41, no. 11, p. 112901, Nov. 2014, doi: 10.1118/1.4896820.

[21] W. Kwiecinski *et al.*, "Cardiac shear-wave elastography using a transesophageal transducer: application to the mapping of thermal lesions in ultrasound transesophageal cardiac ablation," *Phys Med Biol*, vol. 60, no. 20, pp. 7829–7846, Oct. 2015, doi: 10.1088/0031-9155/60/20/7829.

[22] T. D. Bahnson *et al.*, "Feasibility of Near Real-Time Lesion Assessment During Radiofrequency Catheter Ablation in Humans Using Acoustic Radiation Force Impulse Imaging," *Journal of Cardiovascular Electrophysiology*, vol. 25, no. 12, pp. 1275–1283, 2014, doi: 10.1111/jce.12514.

[23] J. Grondin, E. Wan, A. Gambhir, H. Garan, and E. Konofagou, "Intracardiac myocardial elastography in canines and humans in vivo," *IEEE Trans Ultrason Ferroelectr Freq Control*, vol. 62, no. 2, pp. 337–349, Feb. 2015, doi: 10.1109/TUFFC.2014.006784.

[24] E. Bunting, C. Papadacci, E. Wan, V. Sayseng, J. Grondin, and E. E. Konofagou, "Cardiac Lesion Mapping In Vivo Using Intracardiac Myocardial Elastography," *IEEE Transactions on Ultrasonics, Ferroelectrics, and Frequency Control*, vol. 65, no. 1, pp. 14–20, Jan. 2018, doi: 10.1109/TUFFC.2017.2768301.

[25] N. Milani-Nejad and P. M. L. Janssen, "Small and large animal models in cardiac contraction research: Advantages and disadvantages," *Pharmacology & Therapeutics*, vol. 141, no. 3, pp. 235–249, Mar. 2014, doi: 10.1016/j.pharmthera.2013.10.007.

[26] G. E. Billman, "In-Vivo Models of Arrhythmias: a Canine Model of Sudden Cardiac Death," in *Practical Methods in Cardiovascular Research*, S. Dhein, F. W. Mohr, and M. Delmar, Eds. Berlin/Heidelberg: Springer-Verlag, 2005, pp. 111–128.

[27] V. Sayseng, J. Grondin, and E. E. Konofagou, "Optimization of Transmit Parameters in Cardiac Strain Imaging With Full and Partial Aperture Coherent Compounding," *IEEE Transactions on Ultrasonics, Ferroelectrics, and Frequency Control*, vol. 65, no. 5, pp. 684–696, May 2018, doi: 10.1109/TUFFC.2018.2807765.

[28] Enriquez Andres *et al.*, "Use of Intracardiac Echocardiography in Interventional Cardiology," *Circulation*, vol. 137, no. 21, pp. 2278–2294, May 2018, doi: 10.1161/CIRCULATIONAHA.117.031343.

[29] W.-N. Lee, C. M. Ingrassia, S. D. Fung-Kee-Fung, K. D. Costa, J. W. Holmes, and E. E. Konofagou, "Theoretical Quality Assessment of Myocardial Elastography with In Vivo Validation," *IEEE Transactions on Ultrasonics, Ferroelectrics and Frequency Control*, vol. 54, no. 11, pp. 2233–2245, 2007, doi: 10.1109/TUFFC.2007.528.

[30] F. Kallel and J. Ophir, "A Least-Squares Strain Estimator for Elastography," *Ultrason Imaging*, vol. 19, no. 3, pp. 195–208, Jul. 1997, doi: 10.1177/016173469701900303.

[31] A. A. Taha and A. Hanbury, "Metrics for evaluating 3D medical image segmentation: analysis, selection, and tool," *BMC Med Imaging*, vol. 15, Aug. 2015, doi: 10.1186/s12880-015-0068-x.

[32] K. H. Zou *et al.*, "Statistical Validation of Image Segmentation Quality Based on a Spatial Overlap Index," *Acad Radiol*, vol. 11, no. 2, pp. 178–189, Feb. 2004, doi: 10.1016/S1076-6332(03)00671-8.

[33] J. W. Holmes, T. K. Borg, and J. W. Covell, "Structure and Mechanics of Healing Myocardial Infarcts," *Annual Review of Biomedical Engineering*, vol. 7, no. 1, pp. 223–253, 2005, doi: 10.1146/annurev.bioeng.7.060804.100453.

[34] "Monitoring stiffness changes in lesions after radiofrequency ablation at different temperatures and durations of ablation," *Ultrasound in Medicine & Biology*, vol. 31, no. 3, pp. 415–422, Mar. 2005, doi: 10.1016/j.ultrasmedbio.2004.12.020.

[35] J. Grondin, V. Sayseng, and E. E. Konofagou, "Cardiac Strain Imaging With Coherent Compounding of Diverging Waves," *IEEE Transactions on Ultrasonics, Ferroelectrics, and Frequency Control*, vol. 64, no. 8, pp. 1212–1222, Aug. 2017, doi: 10.1109/TUFFC.2017.2717792.

[36] V. Sayseng, J. Grondin, R. A. Weber, and E. E. Konofagou, "A comparison between unfocused and focused transmit strategies in cardiac strain imaging," *Phys. Med. Biol.*, 2019, doi: 10.1088/1361-6560/ab4afd.

[37] T. Dickfeld *et al.*, "Characterization of Radiofrequency Ablation Lesions With Gadolinium-Enhanced Cardiovascular Magnetic Resonance Imaging," *J Am Coll Cardiol*, vol. 47, no. 2, pp. 370–378, Jan. 2006, doi: 10.1016/j.jacc.2005.07.070.

[38] S. A. Eyerly, M. Vejdani-Jahromi, D. M. Dumont, G. E. Trahey, and P. D. Wolf, "The Evolution of Tissue Stiffness at Radiofrequency Ablation Sites During Lesion

Formation and in the Peri-Ablation Period," *J. Cardiovasc. Electrophysiol.*, vol. 26, no. 9, pp. 1009–1018, Sep. 2015, doi: 10.1111/jce.12709.

[39] S. A. Eyerly *et al.*, "Intracardiac acoustic radiation force impulse imaging: a novel imaging method for intraprocedural evaluation of radiofrequency ablation lesions," *Heart Rhythm*, vol. 9, no. 11, pp. 1855–1862, Nov. 2012, doi: 10.1016/j.hrthm.2012.07.003.

[40] C. Ma and T. Varghese, "Comparison of cardiac displacement and strain imaging using ultrasound radiofrequency and envelope signals," *Ultrasonics*, vol. 53, no. 3, pp. 782–792, Mar. 2013, doi: 10.1016/j.ultras.2012.11.005.

[41] R. G. P. Lopata, M. M. Nillesen, H. H. G. Hansen, I. H. Gerrits, J. M. Thijssen, and C. L. de Korte, "Performance Evaluation of Methods for Two-Dimensional Displacement and Strain Estimation Using Ultrasound Radio Frequency Data," *Ultrasound in Medicine & Biology*, vol. 35, no. 5, pp. 796–812, May 2009, doi: 10.1016/j.ultrasmedbio.2008.11.002.

[42] S. K. Alam and J. Ophir, "On the use of envelope and RF signal decorrelation as tissue strain estimators," *Ultrasound in Medicine & Biology*, vol. 23, no. 9, pp. 1427–1433, 1997, doi: 10.1016/S0301-5629(97)00186-5.

[43] W. F. Walker and G. E. Trahey, "A fundamental limit on delay estimation using partially correlated speckle signals," *IEEE Transactions on Ultrasonics, Ferroelectrics and Frequency Control*, vol. 42, no. 2, pp. 301–308, Mar. 1995, doi: 10.1109/58.365243.

[44] H. Blessberger and T. Binder, "Two dimensional speckle tracking echocardiography: basic principles," *Heart*, vol. 96, no. 9, pp. 716–722, May 2010, doi: 10.1136/hrt.2007.141002.